Some Investigations on the Ionosphere during 2012–2014 in China

AUTHORS

LIU Libo[1, 2]
CHEN Yiding[1, 2]
LE Huijun[1, 2]
LIU Jing[1, 2]
WAN Weixing[1, 2]

[1] Key Laboratory of Earth and Planetary Physics, Institute of Geology and Geophysics, Chinese Academy of Sciences, Beijing 100029
[2] Beijing National Observatory of Space Environment, Institute of Geology and Geophysics, Chinese Academy of Sciences, Beijing 100029

ABSTRACT

In this national biannual report, we will outline some recent progresses in ionospheric studies conducted by Chinese scientists since 2012. The mentioned aspects include: (1) the solar control of the ionosphere; (2) couplings between the ionosphere, lower atmosphere and plasmasphere; (3) ionospheric climatology and disturbances; (4) ionospheric irregularities and scintillation; (5) models, data assimilation and simulations; (6) unusual phenomena of the ionosphere; (7) possible seismic signatures presented in ionospheric observations, and (8) some methodology progresses. These progresses will enhance our ability to observe the ionosphere, provide more reasonable understanding about the states of the ionosphere and underlying fundamental processes, and stimulate ionospheric modeling, forecasting and related applications.

KEY WORDS

Ionospheric weather, Ionospheric climatology, Ionospheric storm, Waves

1 Solar Control of the Ionosphere

Solar X-ray and Extreme Ultraviolet (EUV) radiation impacts the upper atmosphere of the Earth, forms the ionosphere and controls the evolution of the ionosphere and the upper atmosphere.

Le *et al.*[1] quantitatively investigated Solar Zenith Angle (SZA) dependence of the Total Electron Content (TEC) enhancements (ΔTEC) during flares by using data from GOES X-ray and EUV and GPS TEC during about 100 X-class flares in 1999–2006. The response of the ionosphere to a solar limb flare is found to be weaker than to a central one. Such a feature is called the CMD effect, which is found to be less distinct with decreasing X-ray class of the flare. The TEC response to flares is closely related to the intensity of EUV flux enhancement, but not highly related to that of X-ray flux. The flare effect is more significant in equinoxes than in solstices, under the influence of the seasonal variation of the background neutral density.

It has potential application to estimate the intensity of a solar flare using ionospheric observations. Xiong *et al.*[2] proposed an ionospheric solar flare indicator in terms of global network TEC observations during 1439 M-class and 126 X-class flares in solar cycle 23 (1996–2008). The indicator enables us to detect the extreme X-class flares, and also flares one order of magnitude or even more weaker (such as C-class flares). The validation shows that the indicator can detect 80% M-class and 92% X-class flares during 1996–2008, but insensitive to some limb flares. The outstanding advantage of the indicator, high sensitivity and temporal resolution, indicates, as Figure 1 illustrated, that it can be utilized to monitor detailed information about solar flares in space weather applications.

The radio wave emission shortly after a solar flare, Solar Radio Burst (SRB), originates from the solar atmosphere. During a SRB event, some specific frequency radio waves could interfere with the signals of technical systems, such as Global Navigation Satellite System (GNSS). Yue *et al.*[3] made case and statistical analyses of the SRB effect on the Radio Occultation (RO) technique during April 2006 to September 2012. RO signals of multiply Low Earth Orbit (LEO) based high-resolution GNSS were used to study the effect of SRB statistically. They showed more details in higher resolution response of RO signals in response to SRB event. The SRB could affect GNSS RO significantly by decreasing data volume and quality.

Ma *et al.*[4] investigated the effect of ~27 day solar rotation on the ionospheric F_2 region peak electron densities (N_mF_2) observed in the East Asian-Australian sector from 1969 to 1986. They found that the ~27 day variations in solar radiation and geomagnetic activity,

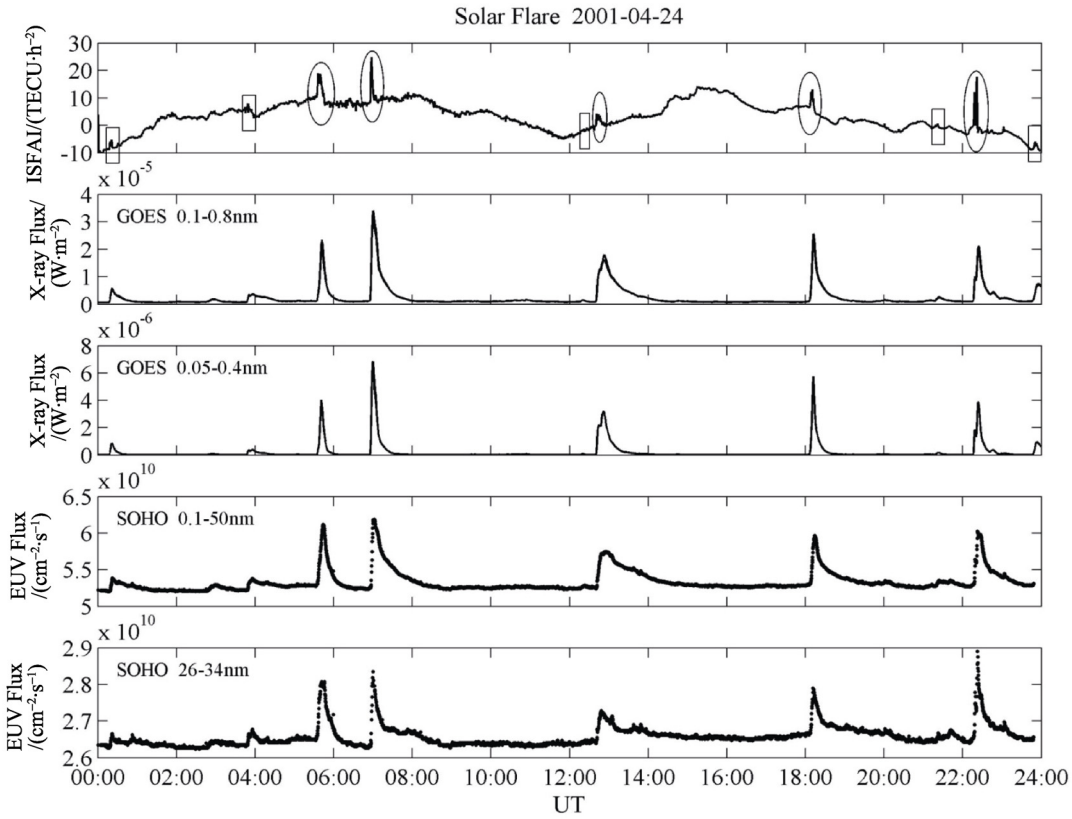

Fig.1 Temporal evolution of the flare indicator and X-ray and EUV fluxes on 24 April 2001[2]

caused by solar rotation, have large impact on the ionosphere, mainly driving the ionospheric ~27 day variations. At low magnetic latitudes, the contribution of solar EUV radiation to the ~27 day variation was greater than that of geomagnetic activity, but the results are opposite at higher latitudes, especially at midnight.

Chen *et al.*[5] investigated the correlations between SOHO/Solar EUV Monitor 26–34 nm EUV and the $F_{10.7}$ and Mg II proxies at timescales of solar cycle (long-term) and solar rotation (short-term). The long-term components of EUV and proxies are well correlated with each other, and the general relation between them can be captured by the 81-day averaged EUV and proxies. Short-term EUV-proxy correlation is poorer and variable during the solar cycle. The slopes of short-term EUV against proxies vary from solar rotation to solar rotation, and they are generally lower than those of long-term. The variability of solar EUV and proxies has significant signatures in the ionosphere. Proxies are improved to effectively capture the variations in EUV, although they cannot follow the short-term variability completely.

The solar activity has an extremely extended low in 2007–2009, with a record of spotless days since the discovery of the ionosphere. It is critical what this deep solar minimum had brought to the Earth's space environment. Liu *et al.*[6] and Yang *et al.*[7] analyzed the DPS ionograms measured at Jicamarca (12.0° S, 283.2° E) to explore what happened in the equatorial ionosphere during the deep minimum. Compared to 1996–1997, the seasonal median values of the critical frequency of F_2-layer (f_0F_2) remarkably reduced during the deep solar minimum. It is the first time to find that decreasing trend prevails in the F_2-layer peak height (h_mF_2) and Chapman scale height (H_m). Furthermore, the electron density profiles retrieved from ionogram demonstrate that the topside ionosphere in 2008–2009 is contracted strongly and more perceptible in the afternoon hours. The decrease in N_e is strongest on September equinox and weakest on June solstice. In contrast, the bottomside profile thickness (B_0) in 2008–2009 shows higher values than that in 1996–1997 in some daytime intervals.

2 Couplings between the Ionosphere, Lower Atmosphere and Plasmasphere

Wan *et al.*[8] numerically investigated the couplings between the non-migrating tide (diurnal eastward wavenumber-3 DE3 tide) in the mesosphere and low thermosphere (MLT) and the response of the upper thermosphere and ionosphere. The tides were included as lower boundary sources to Global Coupled Ionosphere-Thermosphere-Electrodynamics Model developed by the Institute of Geology and Geophysics, Chinese Academy of Sciences (GCITEM-IGGCAS)[9]. The longitudinal wavenumber-4 (WN4) structure in the upper thermosphere and ionosphere was reasonably reproduced by GCITEM-IGGCAS. The simulations with some devised control conditions were used to discuss the relative contributions of the upward tidal wave propagation and the electro-dynamical coupling. Quantitative analysis shows that the electro-dynamical coupling mechanism is responsible for almost all the ionospheric and thermospheric WN4 waves, while the direct wave propagation mechanism is important only for the thermospheric WN4 waves under low and moderate solar activity conditions.

Xiong and Lühr[10] investigated the tidal signatures in the magnitude and the inter-hemisphere asymmetry of the Equatorial Ionization Anomaly (EIA) based on nine years of CHAMP and GRACE observations. Both the EIA magnitude and Crest-to-Trough Ratio (CTR) parameters show WN4/WN3 patterns are dependent on season. The contribution of tidal components to EIA in different months was identified.

Sudden Stratospheric Warming (SSW) is another manifestation of the coupling between the lower atmospheres and the ionosphere. The SSW in the winter of 2008/2009 is the strongest event recorded. Xiong *et al.*[11] found the semidiurnal variation of TEC enhancement with phase shifting forward in Beijing (40.30° N, 116.19° E) during 22 to 27 January 2009. Wind observations from the Beijing all-sky meteor radar illustrated that the semidiurnal solar tide in the mesosphere starts to increase before the SSW and maintains oscillation with period 16–20 days during this period. The phase comparison showed that lunar tides in TEC and zonal wind reach their maxima almost simultaneously, but lag 2–4 h behind the meridional wind. They proposed that the semidiurnal variation of TEC is attributed to the coupling between the mesosphere and ionosphere through both solar and semidiurnal lunar tides, and the enhancement in semidiurnal lunar tide is responsible for the TEC peak's forward shift.

For the 2005–2006 SSW event, Mo *et al.*[12] revealed a quasi-16-day periodicity in the meridional movement of Equatorial Ionization Anomaly (EIA) crest, which is derived from GPS observations at low latitude over China. Such large-scale periodic movement of EIA crest is likely related to the globally enhanced stratospheric planetary waves. The Equatorial Electrojet (EEJ) and

h_mF_2 at two Chinese ionosonde stations also vary in phase with the EIA movement.

Comparing the tide structures and the corresponding signatures in the ionosphere should shed some light on the coupling between the ionosphere-thermosphere and the lower atmosphere. Luan *et al.*[13] derived the latitudinal, seasonal and solar cycle variations of the signature of terdiurnal westward migrating wave number 3 (TW3) tide in JPL TEC during 1999–2011. The TW3 absolute amplitude peaks in the magnetic equatorial region, and the TW3 relative amplitude has a main peak in the magnetic equatorial region and a secondary one at magnetic middle latitudes. Moreover, the relative amplitude of zonal mean TEC in equatorial region shows little solar activity dependence.

Gong *et al.*[14] presented an extensive analysis of atmospheric tides in the low-latitude thermosphere and their responses to a major SSW event (18–23 January 2010). Their analysis was based on the Arecibo dual-beam ISR observations, which overlapped with the SSW event. In order to investigate the thermospheric tidal response to the SSW, nine consecutive days of data were separated into two periods: the non-SSW period and the SSW period. The power spectral density analysis shows several strong tidal components in both periods but with large period-to-period variability. This large variability is most likely due to the effects of the SSW.

Tang *et al.*[15] studied the ionospheric quasi-biennial oscillations (QBO) through analyzing the TEC observations during the period of 1999–2011. QBO signal only appears in TEC during solar maximum, existing at latitudes from 50°S to 50°N with 22–34 months period. In the equatorial region, the QBO exhibits a significant feature of EIA, where the transition of phases occurs 2–6 months later than at high latitude. Stratospheric QBO possibly influences the QBO phenomenon in the ionosphere.

The atmosphere-ionosphere coupling may influence the ionospheric absorption. Hao and Zhang [16] checked the manifestations of atmospheric influences on ionospheric absorption in the East Asia sector. They detected a dominant 27-day periodic variation in the absorption level recorded at Beijing with a sweep frequency technique for 4 years. Unusual enhancements of the absorption level in winters (winter anomaly) vary with periods mainly in the range of 8–12 days. Comparing to the solar 27-day rotation component, the oscillations with shorter periods are related with planetary wave activities in the lower atmosphere.

Chong *et al.*[17] investigated the patterns of the plasmaspheric electron content (PEC) derived from the observations of the incoherent scatter radar (ISR) and GPS at Millstone Hill (42.6°N, 288.5°E). Both PEC and its relative contribution to GPS-TEC exhibit obviously diurnal variations, with higher values and lower relative contribution during daytime than nighttime. The PEC value is higher for the High Solar Activity (HSA) and lower for the Low Solar Activity (LSA). The relative PEC contribution at night can be as high as 60% for HSA and 70% for LSA.

Wang and Lühr [18] performed a statistical study to investigate the seasonal effect of Subauroral Polarization Stream (SAPS) on the ion upflow in the northern hemisphere duskside ionosphere by using two years' DMSP plasma observations. Obvious upflows appear in the topside ionosphere around the SAPS region, indicating an important relationship between SAPS and the local plasma upward motion. Both SAPS and ion upward velocities show similar seasonal variations, largest in winter and smallest in summer, irrespective of geomagnetic activity. The SAPS-related frictional heating at mid-latitudes play an important role in the local formation of the strong upward flow, which might provide a direct ionospheric ion source for the ring current and plasmasphere in the duskside sector.

Dispersive Alfven Waves (DAWs) play a significant role in auroral generation of the magnetosphere-ionosphere coupling system. Zhao and Lu[19] showed that dispersive standing Alfven waves can generate the field-aligned currents which transport energy into the auroral ionosphere, where it is dissipated by Joule heating and energy lost due to electron precipitation. The Joule dissipation can heat the ionospheric electrons and influence the ionospheric Pedersen conductivity. The conducting ionosphere can also strongly affect the magnetospheric currents. The ponderomotive force can cause the plasma to move along the field line, and generate ionospheric density cavity. The nonlinear structuring can lead to a dispersive scale to accelerate auroral particle, and the Alfven waves can be trapped within the density cavity.

3 Ionospheric Climatology

In the middle latitude regions over America, the ionosphere over the east and west coast exists significant differences. The configuration of the geomagnetic field is proposed to be the main controller of the neutral field effect. Zhao *et al.*[20] showed that strong east-west differences (R_{ew}) also exist in the ionosphere over the Far East zone,

where a clear diurnal variation is quite similar to that in US. New features over Far East zone include: (1) The noontime negative R_{ew} is most pronounced in April–June, while in US during February-March; (2) The positive R_{ew} at night is much less evident than in US, especially no winter enhancement; (3) The magnitude of negative Rew tends to enhance toward solar maximum and the trend reverses in US.

Xu *et al*.[21] compared the east-west differences of the mid-latitude TEC in North American, South American and Oceania regions. They used ground-based networks of TEC data covering about a solar cycle from 2001 to 2010. Their results show that, for nearly all seasons from 2001 to 2010, systemic differences exist in mid-latitude TEC in both sides of the three zero declination longitudes. The east-west differences vary markedly with local time but depend weakly on season and level of solar activity. Theoretical analysis confirms that the effects of the longitudinal variations of both declination and zonal wind are well consistent with the observed differences of TEC in both sides of the zero declination longitudes.

Xu *et al*.[22] collected the N_mF_2 data from 33 stations in three longitude sectors from 1969 to 1986 to study the seasonal variation of N_mF_2. There is a ter-annual variation in daytime N_mF_2, especially at middle latitude, but no obvious ter-annual oscillation signature in the nighttime. The ter-annual amplitude is also correlated with the product of the amplitudes of annual and semiannual oscillations, which suggests that the ter-annual oscillation might be related to the nonlinear interaction between the annual and semiannual oscillations. These three oscillations vary with solar activity, with larger amplitudes during solar maximum.

The possible differences of the ionosphere in two equinoctial seasons are named the equinoctial asymmetry. Chen *et al*.[23] collected the data of several solar cycles of N_mF_2 and one solar cycle of JPL TEC maps to investigate the equinoctial asymmetries in ionospheric electron density and its solar activity dependency. They found different latitudinal patterns of solar cycle dependency of equinoctial asymmetry in noontime N_mF_2 and TEC. With increasing solar activity, the equinoctial asymmetry TEC becomes stronger at all latitudes, while that of N_mF_2 increases at middle latitudes, decreases or changes little at low latitudes. The solar sensitivity of N_mF_2 and TEC also shows equinoctial asymmetries.

Xiong *et al*.[24] studied the morphology of the Equatorial Ionization Anomaly (EIA) at CHAMP (~400 km) and GRACE (~480 km) altitudes, focusing on the magnitude and inter-hemispheric asymmetry of EIA. About nine years (2001–2009) of observations from CHAMP and GRACE were analyzed. The electron density and the magnetic latitudes of the EIA crests both peak around 14:00 LT, while the EIA CTR peaks much later. The magnetic latitude of the EIA can reach 13° at CHAMP altitude around December solstice, while the crests move much closer to the dip equator at GRACE altitude during low solar activity years. An inter-hemispheric asymmetry can be seen clearly in solstice EIA. At CHAMP altitude the EIA has higher electron density in the winter hemisphere during morning to noontime hours and subsequently in the summer hemisphere. At GRACE altitude, the electron density of the EIA crest is always stronger in the summer hemisphere at the whole daytime. The SAMI2 simulations can reproduce such features at the two altitudes.

The north-south asymmetry of the EIA can be explored using the TEC observations from the IGS GPS network. Huang *et al*.[25] examined the hemispheric asymmetry in the EIA crest regions in the 110°E longitude sector under geomagnetic quiet conditions during the period from 2000 to 2011. The strength, latitude and occurrence time of the EIA crests are found to be asymmetric about the magnetic equator. The solar activity levels have a significant effect on EIA crest and the north-south asymmetry.

Wu *et al*.[26] explored the variations of TEC in 2004 over China using the TEC observed from China Crustal Movement Observation Network. The diurnal pattern has a peak in post-noon hours, and the seasonal variation peaks around equinox months. The TEC has higher values with decreasing latitude, and obvious moderate longitudinal differences in both sides of the zero magnetic declination longitude. The day-to-day variation of TEC is less significant than that of N_mF_2.

Xiong *et al*.[27] compared the predictions of the International Reference Ionosphere (IRI-2007) model with the CHAMP and GRACE in-situ measurements for the years from 2005 to 2010 in the subauroral regions. N_e in the trough region peaks in local summer and attains valley in local winter. Around 100°W and 60°E, two larger electron density sectors feature can be seen in both hemispheres, which attributed to the electron extending from middle latitude to trough region. The IRI generally overestimates N_e in the trough region. In detail, the model predicts quite well in the southern hemisphere and needs significant improvement in northern hemisphere.

4 Ionospheric Disturbances

Severe space weather events may drive strong disturbances

in the ionosphere, which seriously influence accurate navigation, telecommunication, and other applications. With the development of ground and space observation techniques, various efforts have been made to understand the long-term statistical variations and sudden disturbances of the ionosphere. Xiao *et al.*[28] outlined some progresses of researches on ionospheric disturbances achieved in recent years.

Large-Scale Traveling Ionospheric Disturbances (LSTIDs) are the ionospheric manifestations of Atmospheric Gravity Waves (AGWs), which were launched from intense high latitude sources, such as Joule heating and particle precipitation. Song *et al.*[29] studied the global propagation features of the LSTIDs during the 7–10 November 2004 magnetic storm, and found that the horizontal phase velocities of LSTIDs were different among different regions, and the attenuations of the daytime LSTID amplitude were larger than the nighttime ones. Song *et al.*[30] analyzed the LSTIDs in China during the 28 May 2011 geomagnetic storm. Two LSTIDs were detected: one is propagating northeastward in southwestern China, and the other is propagating southwestward in northeastern China. The observations of Song[29–30] reflect the variation of the propagation properties of LSTIDs with respect to latitude and local time. During the medium storm on 28 May 2011, a substorm onset and initiated a slow-speed LSTID over North America just after midnight[31]. Several hours after that, Ding *et al.*[31] observed two LSITDs in East Asia using data from Chinese GPS network, combined with observations from an ionosonde chain. Although the nighttime LSTID over China travelled farther south than the earlier dusk event, both disappeared in South China. This was due to an increase of the attenuation and uplift of the ionosphere at low latitudes; both resulted in reduced amplitude of TEC perturbations.

Ding *et al.*[32] compared two poleward-propagating LSTID cases during a moderate storm. The observations from the GPS network and ionosondes in China and Southeast Asia display a northeastward-propagating LSTID in the 30 May morning and the other during the nighttime of 1 June. Both LSTIDs occurred during the storm's recovery phase and experienced severe dissipation. Although the relative amplitude of the nighttime LSTID was ~60% larger than that of the morning event initially, strong ion-drag dissipation induced by a strong nighttime enhancement in background TEC led to dissipation quicker than the morning event. Therefore, poleward propagating LSTIDs were likely excited by some local sources, possibly excited through the dissipation of some primary medium-scale disturbances from the lower atmosphere.

Ding *et al.*[33] conducted a comparative study of the climatology of LSTIDs over North America and China in 2011–2012 based on the GPS observations from two dense regional coverage networks. They identified a total of 390 LSTIDs in China and 363 events in North America. These LSTIDs were categorized into three types, according to the propagating directions. The southward LSTIDs over North America show similar diurnal and seasonal variations to those of geomagnetic disturbances, but over China such type LSTIDs do not show the similar variations. Northward LSTIDs occur much less frequently and are mainly observed in China. Westward LSTIDs are seen in both regions during local sunrise and may be excited by the moving solar terminator. The propagation direction of westward events changed from northwestward during winter solstice to southwestward in summer solstice, which is consistent with the seasonal orientation of the solar terminator.

Song *et al.*[34] further statistically studied the LSTIDs triggered by the solar terminator over China. The occurrence rate of LSTIDs has maximum in winter and minimum in summer, and the propagation direction shows a highly seasonal dependence.

Cai *et al.*[35] presented further observational evidence for the transpolar propagation of LSTIDs from their nightside source region to the dayside reported earlier. Slant TEC (STEC) from GPS receiver chains longitudinally aligned in North American and European sectors was analyzed to demonstrate presences of LSTIDs in both nightside and dayside mid-latitude. The derived periods of the ionospheric disturbances are in good agreement with that of the transpolar AGW recorded by EISCAT/ESR radars. The observed daytime and nighttime mid-latitude LSTIDs are likely to origin from auroral latitude. After launched from the nightside, the waves propagate simultaneously equatorward and poleward, which are recorded by North American GPS receiver chain and by EISCAT/ESR radars and GPS receiver chains, respectively.

The zonal electric field strongly modulates the low-latitude ionosphere, especially under disturbance conditions. Sun *et al.*[36] compared the disturbance vertical drift in ionospheric F layer during the initial and main phases of 50 intense storms in terms of historical ionosonde data observed at Haikou and Chongqing. The disturbance drift is taken from an empirical model. The drifts at the base and peak height are comparable and both increase in magnitude under stronger disturbances. Moreover, drifts over Haikou are larger than over

Chongqing.

A positive ionospheric storm occurred during the main phase of the 20 November 2003 superstorm. Zhao *et al*.[37] investigated this event using observations from ground-based GPS TEC and the meridian chain of ionosondes distributed along the Latin America longitude of ~280° E. At mid- and low latitudes the maximum enhancement is 3.2–7.7 times in the topside ionospheric electron content compared to the bottomside. Moreover, h_mF_2 at middle to low latitudes exceeds 400 km and increases by 100 km compared with that on the quiet day over the South American area, which might be resulted from a continuous eastward penetration electric field and storm-generated equatorward winds.

Wu *et al*.[38] studied the high energy particle precipitation effects in Arctic ionosphere during the main phase of the 14–15 December 2006 magnetic storm. Observations are from GPS TEC, EISCAT radar, RO from both CHAMP and COSMIC, and the ionospheric absorption of cosmic radio noise measured by the Imaging Riometer for Ionospheric Studies at Kilpisjärvi (69.05°N, 20.79°E). During the main phase, significant increases in electron density were found in the Arctic ionosphere, in Scandinavian, Northwest part of Russia and Svalbard (SNRS) regions. Increase in electron density is primarily at an altitude of about 110 km. The increases were accompanied by the ionospheric absorption enhancement at altitude of about 90 km. The observations provide direct evidence that the storm-time enhancement in E-layer electron density (*e.g*., the sporadic E) can contribute dominantly to the observed TEC increase.

Luan *et al*.[39] performed a superposed epoch analysis to investigate the relative impact of the solar wind/ Interplanetary Magnetic Field (IMF) on geomagnetic activity, auroral hemispheric power, and auroral morphology during Corotating Interaction Regions (CIRs) events between 2002 and 2007. They compared the CIRs effects under different solar wind/IMF conditions. Interesting auroral morphology is found around CIR onset time. Their work suggests during CIR events, southward B_z plays the most critical role in determining geomagnetic and auroral activity, whereas solar wind speed is the next most important contributor. The solar wind dynamic pressure is the least important factor, as compared with B_z and solar wind speed.

The observations of CHAMP thermospheric mass density (normalized to 400 km) during 2001–2008 and TIMED/GUVI O/N_2 from 2002 to 2008 are used by Liu *et al*.[40] to investigate the solar cycle and seasonal dependencies of the thermospheric response to CIRs. The relative changes of the thermosphere vary with solar cycle, decreasing pronouncedly in neutral density and increasing in high latitude O/N_2 at higher solar levels. The relative deviations present a seasonal asymmetry. On the dayside, the peak increases of neutral density at high latitudes in average are higher in the summer hemisphere than in the winter hemisphere. In addition, neutral density changes are more remarkable at nighttime than at daytime.

To estimate the high-speed stream influence on the ionosphere during the recent deep solar minimum year 2008, Liu *et al*.[41] analyzed the equatorial f_0F_2, h_mF_2 and TEC in the American sector. Their results reveal a prominent 9-day oscillation in dip equatorial h_mF_2 and f_0F_2, whose amplitudes are not always positively correlated with those of TEC. The band-passed-filtered TEC displays latitudinal patterns, including tilt latitudinal configuration, opposite correlation between the crests and trough, and south-north asymmetry.

Knowledge of the solar sector polarity effects on the ionosphere may provide some clues in understanding the day-to-day variability and "hysteresis" effect of the ionosphere. Liu *et al*.[42] made a comprehensive investigation on the ionospheric response to changes in solar sector polarity in terms of solar cycle, season and local time dependencies. The solar sector polarity effect is more appreciable in equinoctial months than in solstitial months, which is mainly caused by larger southward B_z components in equinox.

Several solar events occurred on November 6–10, 2004, including solar flares and Coronal Mass Ejections (CMEs), which triggered two large geomagnetic storms and continuous energy proton events. Zhang *et al*.[43] detected that, in the East-Asian region, a large positive ionospheric storm happened on November 8 and strong spread-F at mid-latitude appeared on November 10. They took the Rate of TEC (ROT) derived from dual-frequency GPS measurement to study the characteristics of the spatial distribution of the ionosphere fluctuations and their temporal evolution. Strong fluctuating activity in the ionosphere occurred in the mid-latitude regions between longitudes of 100°E and 180°E in both hemispheres.

A long-lasting southward turning of Interplanetary geomagnetic Field (IMF) for 30 h below −10 nT triggered a major geomagnetic storm on July 15–16, 2012. Wang *et al*.[44] observed prominent large-scale ionospheric disturbances in North China during this storm event. They used the newly built China Seismic-ionospheric Ground-based Monitoring Network (CSGMN), including GPS network and oblique and vertical sounding systems, to investigate the ionospheric responses at different storm phases. A moderate and a strong positive storm

were observed around the noon and the sunset sector on 15 July, respectively. Then, an intense negative storm effect occurred on the entire day of July 16.

Xiao *et al*.[45] reconstructed the low-latitude electron density distributions during the November 2004 superstorm from GPS observations of ground-based IGS network and onboard CHAMP and GRACE satellites using time-dependent 3D tomography method. The reconstructed electron densities are validated with CHAMP and GRACE in situ measurements. The long-lived positive storm phase during the first main phase of the storm (November 8) is mainly attributed to enhancement of electron density in the upper F region. The top-hat-like double layers occurred in the equatorial ionization anomaly region during the main phase of the storm. At the time of the minimum of *Dst* The column-like enhanced electron density structures are found in the longitudinal sector about 157°E, which extend from the topside ionosphere toward plasmasphere, reaching at least about 2000 km as high. Their footprints stand on the two peaks of the EIA.

Xiong *et al*.[46] investigated the relationship between the polar cap potential and its temporal variation rate and the disturbed equatorial ion velocity during 2001 to 2003. The equatorial vertical ion drift is measured by DMSP, and polar cap potential from AMIE output. Their analysis indicates that the electric field penetrates more easily under rapidly varying solar wind input. The optimal delay time of electric field penetration from the high-latitude magnetosphere to equatorial ionosphere has local time dependence, being longer at nightside. The penetration efficiency is lower at day than at night.

5 Ionospheric Irregularities and Scintillation

A VHF coherent scatter radar with frequency of 47.5 MHz and peak power of 24 kW has been operated since February 2009 at Sanya (18°N, 109°E, dip 13ºN), a southern city of Hainan Is., China. The characteristics of Field-Aligned Irregularities (FAIs) in the low latitude ionosphere have been extensively studied using the observations of the Sanya VHF coherent radar. Several interesting aspects of the FAIs observed include the E-region continuous[47–48] and quasi-periodic FAI echoes[49], the post-midnight F region FAIs[50], and the Range Spread Trail Echoes (RSTEs) produced by meteoroid ablation [51].

Li *et al*.[52] analyzed the data from the continuous observations of F region irregularities by the Sanya VHF radar, an ionosonde and a GPS scintillation/TEC receiver during the equinoctial and June solstitial months of 2009–2010. The F region 3 m FAIs appeared frequently at post-sunset hours in equinox, but initiated mostly at midnight/post-midnight in June solstice. Comparison of FAIs observed from GPS scintillations, TEC fluctuations and spread-F shows that the equinoctial FAIs coincided well with GPS scintillations and TEC fast depletions, which are associated with the development of Equatorial Plasma Bubbles (EPBs). For the June solstitial FAIs, satellite in-situ measurements show that some post-midnight FAI structures over Sanya may originate from equatorial region and then extend to Sanya latitude along magnetic field lines, and the others have local origins. Both types of post-midnight FAIs in June solstice are associated with the occurrence of spread-F, not accompanied by GPS scintillations and TEC depletions.

In attempts to understand the day-to-day variability in Equatorial Spread-F (ESF), studies in recent years have revealed the role of seeding perturbation as a dominant source of such variability. Using the Sanya VHF radar five-beam scanning measurements in east–west direction, Li *et al*.[53] investigated the correspondence between the Large-Scale Wave Structures (LSWS) and the development of ESF over Sanya. The LSWS and ESF have nearly a one-to-one relationship when the F layer undergoes an abrupt Post-Sunset Rise (PSSR). However, under weak or even moderate PSSR conditions, more factors other than the LSWS could play crucial roles favoring the growth of ESF instabilities responsible for ionospheric scintillations. Further, Li *et al*.[54] conducted simultaneous ESF backscatter plume observations using the Equatorial Atmosphere Radar and the Sanya VHF radar to investigate the temporal and spatial evolutions of plumes and their smaller scale longitudinal differences in Southeast Asia. The simultaneous radar beam steering measurements revealed that the LSWS could trigger the sunset equatorial plasma plumes occurring quasi-periodically at a wide longitudinal span of about 25°. On the other hand, the observations indicated that the small-scale waves, unlike the LSWS which occurred at a larger longitudinal span of more than 1000 km, might occur only at a narrower longitudinal range. It is quite possible that the appearance of small-scale wave structure in the bottomside F region may be required for further evolution of bottomside spread F or plumes under weak PSSR.

Luo *et al*.[55] investigated the three-dimensional linear growth rate of Rayleigh-Taylor (R-T) instability. The peak growth rate of the R-T instability significantly relies on local time, season, solar activity and longitude,

displaying similar characteristics with that of the irregularities and scintillations in equatorial and low-latitude ionosphere. Therefore, the peak growth rate can be used to indicate the occurrence of the ionospheric irregularity and scintillation.

Luo *et al.*[56] studied how the hemispheric asymmetry of the background ionosphere and the longitudinal variations of neutral wind and declination influence the development and evolution of generalized R-T instability. They adopted the method of flux-tube integration in each geomagnetic hemisphere. The flux-tube integrated linear R-T instability growth rate shows significant hemispheric asymmetry, and the neutral wind with hemispheric asymmetry may result in an asymmetric distribution of ionospheric irregularities. Longitudinal variations of the neutral wind and the declination could cause the longitudinal variation of ionospheric irregularities.

Five years of CHAMP Fluxgate Magnetometer (FGM) data were analyzed by Xiong *et al.*[57] to investigate the characteristics of Equatorial Plasma Bubbles (EPBs). Band-passes with four different cut-off periods were used to filter the FGM data to retrieve the EPBs with selected spatial scale sizes in the meridional plane ranging from 76–608 km. By comparing the properties of EPB occurrence for different scale sizes with the global distribution of plasma vertical drift from ROCSAT-1, they found that EPBs reaching higher altitudes are more structured than those sampled near the topside of the depleted fluxtube. Small-scale EPB structures are observed by CHAMP, primarily in the Brazilian sector around November, with high post-sunset vertical plasma drift.

A puzzling phenomenon in the daytime equatorial ionosphere is the so-called 150 km coherent backscatter echoes induced by the irregularities in the height range of 140–180 km. Using the Sanya VHF radar measurements, Li *et al.*[58] presented first results of daytime 150 km echo from a magnetic latitude close to the northern anomaly crest region. It is found that the rare observation of daytime 150 km echoes with the Sanya VHF radar was preceded by the occurrence of an unusual intermediate layer, which is identified as abnormal traces at the upper E region in corresponding ionograms. They suggested that the critical conditions favoring the irregularity growth were linked with the upper E region abnormal density layer traces that were possibly associated with gravity wave activity.

A layered model was taken by Shi[59] to analyze the influence of electrical conductivity and magnetic dip angle on the Ionospheric Alfven resonant (IAR) feedback instability. Numerical calculations show that the dip angle effectively modifies the resonant frequencies and growth rate of the IAR, which consequently influence the IAR feedback instability. Considering Hall conductance can increase the growth rate, especially for large dip angle.

6 Models, Data Assimilation and Simulations

Ren *et al.*[9] further developed ionospheric theoretical model, and built a new three-dimension mid- and low-latitude theoretical ionospheric model, named Three-Dimension Theoretical Ionospheric Model of the Earth in the Institute of Geology and Geophysics, Chinese Academy of Sciences (TIME3D-IGGCAS). The new model covers the domain of mid- and low-latitude ionosphere and whole plasmasphere, self-consistently solves the equations of mass continuity, motion and energy of electron and ions to provide the main ionospheric and plasmaspheric parameters (number density, velocity, and temperature) in a realistic configuration of the geomagnetic field.

Ren *et al.*[60] simulated the temporal-spatial distribution of the summer nighttime anomaly at mid-latitude (MSNA) and the influences of thermospheric meridional and zonal winds on the formation of MSNA using the TIME3D-IGGCAS. In their simulations, MSNA mainly appears in three regions, East Asia, North Atlantic-Europe and the South Pacific region, in local summer, also frequently in equinox. MSNA in the third region is obviously stronger than in the other regions. The formation of MSNA is mainly related with the meridional wind, and the zonal wind also plays an important role in the South Pacific region.

The vertical drift plays a key role in forming of the equinoctial asymmetry of the low latitude ionosphere. Ren *et al.*[61] simulated how the equatorial vertical drifts are influenced by lower thermospheric tidal winds using the TIDM-IGGCAS-II model. The tidal winds below 105 km are taken from TIMED/TIDI observations. The simulations show larger daytime vertical drift in March Equinox than in September Equinox in most longitudinal sectors. Asymmetry in daytime vertical drift is stronger in the eastern hemisphere than in the western hemisphere, which is driven by DW2 tides and geomagnetic fields. Moreover, the DE3 tides drive the equinoctial asymmetry in the wave number 4 structures in vertical drift.

Yue *et al.*[62] constructed a global ionospheric data assimilation model based on empirical models and the Kalman filter. They performed a series of simulations based on observing systems. A sparse matrix method is

used to relief the huge computation and storage problems. The slant TEC from various ground-based, low-Earth orbit satellites, and cross-link between COSMIC-2 low and high inclination satellites are also simulated. The joint system shows huge impact in specifying the ionosphere. Especially, the COSMIC-2 mission can potentially complement and optimize the global ionospheric specification, contributing significantly to accurate ionospheric nowcasting.

Based on a two-layer Empirical Orthogonal Function (EOF) technique, Zhang *et al.*[63] built an updated global model of h_mF_2 by combining data from COSMIC/FORMOSAT-3 RO measurements and from global ionosonde stations (including 10 Chinese stations). Their model reproduces reasonably well, compared to the measurements of COSMIC RO and digisondes, and it also has a better performance than the well-known International Reference Ionosphere (IRI) model.

Yu *et al.*[64] proposed a technique based on Canonical Correlation Analysis (CCA) to estimate N_mF_2 at a single station or globally from TEC. At a single station, the obtained CCA modes consist of the patterns and corresponding amplitudes, which reflect the short-term and long-term variations of N_mF_2. This method can reasonably estimate the missing values of N_mF_2 at a single station from continuous measurements of the TEC. Global maps of N_mF_2 (N_mF_2-GIMs) can be constructed with the global ionospheric maps for TEC (TEC-GIMs), successfully reproducing their temporal and spatial structures. Furthermore, the correlation coefficient (root mean square error) of the CCA N_mF_2 versus the observed N_mF_2 is relatively higher (lower) than that of IRI-07 N_mF_2 over global stations (Figure 2).

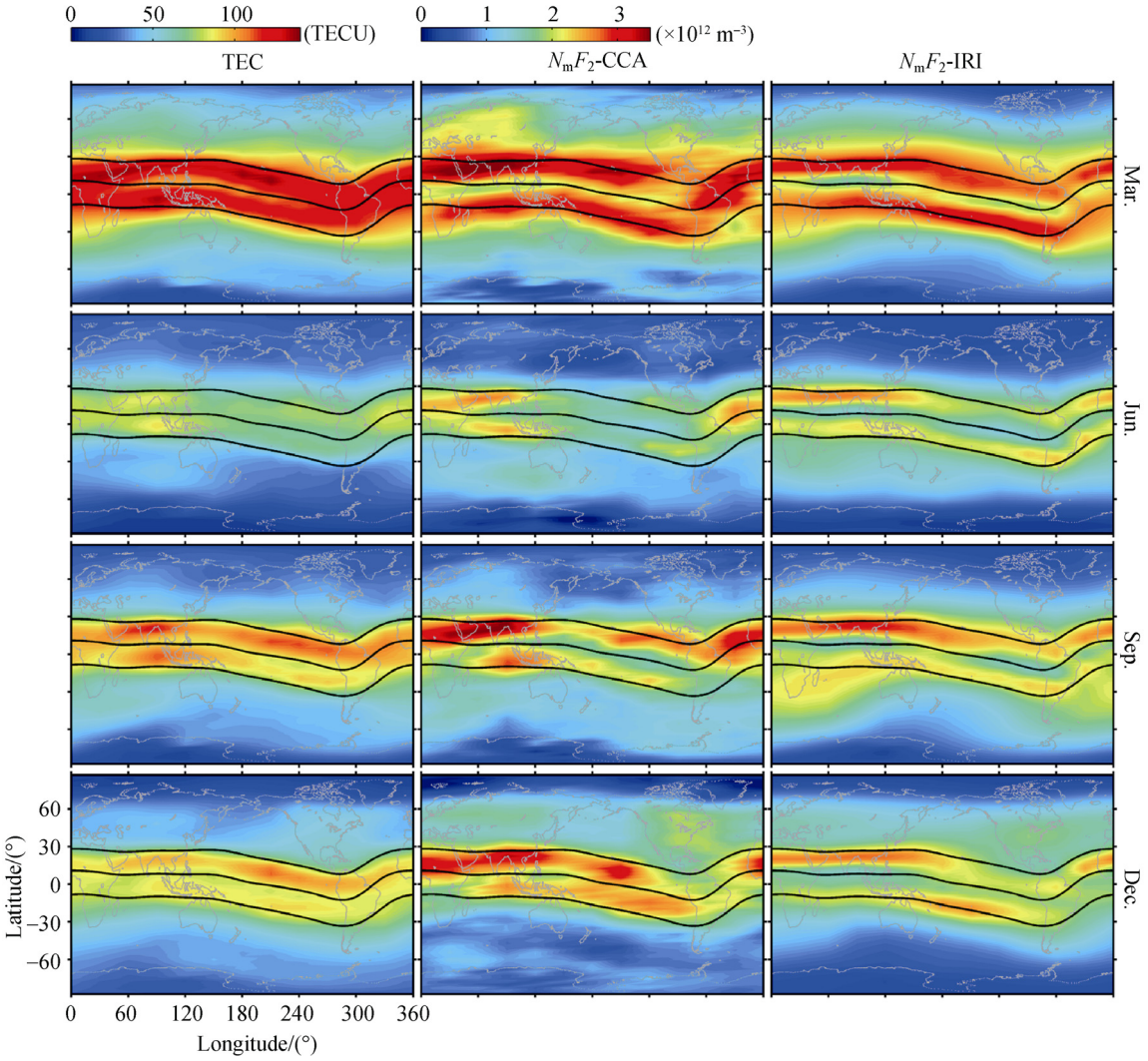

Fig.2 JPL TEC-GIMs (the left column) and N_mF_2-GIMs modeled by CCA (middle) and IRI-07 (right) at 14:00 MLT for March (top row), June (second), September (third), and December (bottom) in 2000

Wan *et al.*[65] adopted Empirical Orthogonal Functions (EOF) to model the global TEC through separating the temporal and spatial variation of TEC into some eigen modes and their amplitudes. The eigen modes give the mapping patterns (latitude and longitude) of TEC, and the corresponding amplitudes depict the variations at different time scales (the solar cycle, annual and semiannual, and the diurnal universal time variations). It is found that the first two modes capture most of the ionospheric climate properties. The EOF analysis has outstanding advantages in ionospheric climatology modeling. A similar model was also built[66].

Liu *et al.*[67] constructed a middle-latitude single station model based on a long-term dataset of hourly values of f_0F_2 recorded at Wakkanai (45.4°N, 141.7°E). The model consists of two modules, geomagnetic quiet and active modules. The geomagnetic quiet module incorporates local time, seasonal, and solar variability of climatological f_0F_2 and its upper and lower quartiles. It is the first attempt to predict the upper and lower quartiles of f_0F_2 to account for the notable day-to-day variability in ionospheric f_0F_2. In the geomagnetically disturbed module, the storm-induced deviations are described by diurnal and semidiurnal waves modulated by a magnetic activity index, reflecting the delayed responses of f_0F_2 to geomagnetic activity forcing. The introduced Kalman filter algorithm optimizes the coefficients of the model in real time. Their model demonstrated that introducing the Kalman filter algorithm is promising for improving the accuracy of short term ionospheric predication.

Sun *et al.*[68] established an empirical model for real-time ionospheric correction, using the nonlinear relations between ionospheric f_0F_2 data from two low-latitude ionosondes and equatorial disturbance field data from an empirical model during fifty storms. They evaluated the performance of the model during twelve intense storms compared with another empirical correction model, STORM. The comparison of the performance of the models indicates that including the disturbance electric fields is important for improving the storm-time ionospheric corrections at low latitude.

Zhao *et al.*[69] constructed a model for 1-hour ahead prediction of f_0F_2 with the AdaBoost-BP algorithm. In their model, twenty-two years' f_0F_2 data from nine ionosonde stations in the East-Asian sector are used. The introducing of the AdaBoost method improves the modeling/prediction of ionospheric parameters, compared to BP Neural Network, Support Vector Regression and the IRI model.

Wang *et al.*[70] explored the diurnal and seasonal variations of ionospheric profile parameter B_{2bot} at Hainan station under low solar activity conditions. They used a local time function in different seasons to correct the B_{2bot} formula of NeQuick-2 to improve its performance.

Based on the EISCAT Svalbard Radar (ESR) observations, He *et al.*[71] analyzed the diurnal variations of N_mF_2 in a solar minimum year 2007. The soft precipitation electron had an evident effect on the N_mF_2 over ESR. The number of electrons in lower energy band becomes less under more active geomagnetic disturbances, resulting in a lower N_mF_2. A comparison is conducted between the IRI model and observations, which illustrates that the IRI model has a better N_mF_2 prediction when the photoionization is dominant and becomes worse when the electron precipitation is dominant.

Shi *et al.*[72] constructed a one-dimensional kinetic model to simulate the electron acceleration by inertial Alfven waves. The cold and hot electrons are treated separately. The including of cold electrons brings intense variation of Alfven speed. The model results show that the exponential decrease of the plasma density leads to the sharp gradient in both Alfven velocity and electron inertial length. When Alfven waves encounter such sharp gradient at lower altitudes, the electrons are accelerated by the waves and become super-Alfvenic, and the width of burst structures becomes much wider than the electron inertial length. Consequently, the background electrons carry the opposite field-aligned current due to plasma oscillation. The electron carried current exceeding the wavefront is balanced by the reverse current carried by background electrons, which reasonably explains observations of the electron bursts accompanied by little net field-aligned current. Furthermore, there is another type of Alfven wave reflection due to mirror force and wave-particle interaction.

7 Unusual Phenomena of the Ionosphere

The F_3 layer is a distorted ionospheric height structure in ionograms. Zhu *et al.*[73] analyzed the features of F_3 layer at low latitude under low and moderate solar activity conditions. The F_3 layer signature was more distinct in spring to summer and less distinct during LSA periods. The ionograms were recorded at a low latitude ionosonde in 2010–2012. They found that the average duration time of the F_3 layer becomes longer and the differences between $h'F_2$ and $h'F_2$ show a

semiannual variation more significantly with increasing solar activity level.

Zhu *et al.*[74] outlined morphological features of the F_3 layer traces in magnetic equatorial (Kwajalein) and low-latitude (Sanya) regions under geomagnetically quiet conditions. They found two formation patterns in F_3 layer. When the F_3 layer appears, the F_3 peak density may increase, with upward moving of the peak of F_3 layer. The F_3 peak density for the second type changes little, even decrease. This work fixed the previous view that the occurrence of the F_3 layer is always accompanied by the density-enhanced region.

The F region electron density occasionally rises pronouncedly during the nighttime, which are termed ionospheric nighttime enhancements. The post-midnight enhancement is an unresolved issue in ionospheric physics. Liu *et al.*[75] analyzed the manually scaled ionograms, which were measured by a Lowell DPS-4D ionosonde operated at Sanya, to explore post-midnight enhancement events occurred in 2012, a year of moderate solar activities. Outstanding features in these cases (see Figure 3) over Sanya include, post-midnight enhancements have a high occurrence, lower h_mF_2 and sharper profiles accompanying the rise in f_0F_2, and earlier rise in electron density at higher altitudes. Moreover, downward plasma drift is detected under the enhancement event, revealing the essential role of the westward electric field in forming the post-midnight enhancements in electron density of ionospheric F-layer at such low latitudes. In contrast, former investigations thought the equatorward winds driving plasma upward, which forms the nighttime enhancement.

The 15 January 2010 solar eclipse swept over Asia around sunset. Two ionosondes at Wuhan and Beijing and an oblique incidence ionosonde network in North China were operated to measure the ionospheric response to the solar eclipse by Chen *et al.*[76]. Strong premidnight and postmidnight enhancements appeared in the ionosphere. The two enhancements were resulted from the plasma flux downward from the top ionosphere, possibly due to the steep decrease of the ionospheric electron density and plasma temperature during the solar eclipse. The different magnitudes of greatest eclipse in the umbra and outside may explain the different occurrence times of the plasma flux.

The Weddell Sea Anomaly (WSA) appeared to be an extreme manifestation of the longitudinal variations in the Southern Hemisphere. Luan and Dou [77] analyzed the longitudinal variations of the nighttime N_mF_2 at southern midlatitudes using the COSMIC observations between 2006 and 2008. Significant longitudinal difference relative to the minimum density prevails in all seasons, although the WSA is only evident in summer under this solar minimum condition. In summer, the maximum longitudinal differences occur around midnight rather than in the evening. The maximum longitudinal differences are associated with the strongest wind-induced vertical plasma drifts in the Western Hemisphere.

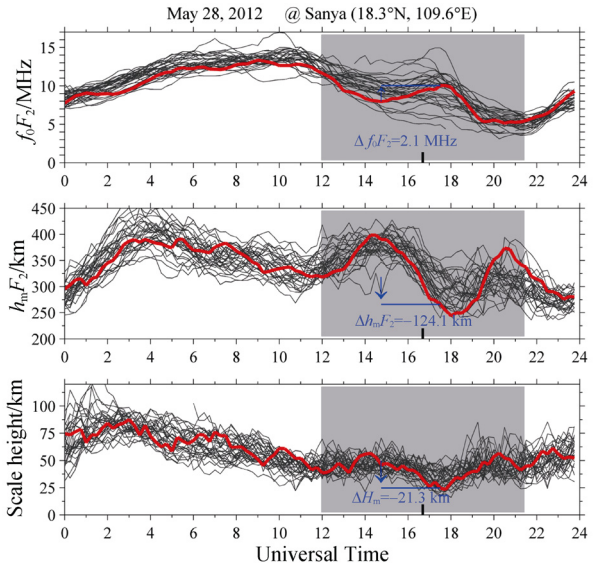

Fig.3 Mass plot of f_0F_2, h_mF_2, and H_m (Chapman scale height) of F-layer observed at Sanya in May 2012. The red line gives the values on May 28th and the black curves plot the values on individual 31 days in that month. In each panel the grey shaded area indicates the interval of local nighttime and the short black bar marks local midnight. The blue arrow shows the onset time of the enhancement in f_0F_2 on May 28th and the horizontal line gives the duration of the f_0F_2 enhancement at the development phase. Δf_0F_2, Δh_mF_2, and ΔH_m are the change of f_0F_2, h_mF_2, and H_m at the enhancement peak from the onset time, respectively [75].

Nighttime ion temperature in the F region is generally thought to be close to neutral temperature. The similarities and differences of the nighttime ion and neutral temperatures in the F region over Millstone Hill were examined by Ruan *et al.*[78] using the incoherent scatter radar and Fabry-Pérot interferometer observations during the periods of 1–11 August 2011 and 12–23 January 2012. Their results showed that in winter, both neutral and ion temperatures exhibited the postmidnight enhancements, which occurred during 03:00 LT–04:00 LT and had amplitudes of about 30–90 K. The extension of midnight temperature maximum over Millstone Hill is the preferred mechanism for the observed enhancements of neutral temperature in winter and summer.

8 Possible Seismic Signatures Presented in Ionospheric Observations

Le *et al*.[79] explored the ionospheric abnormal behaviors prior to the 2011 Tohoku-Oki earthquake. A significant TEC enhancement was present on March 8, 2011. Unfortunately, the solar activity increased during that period. The TEC 30 days before the earthquake was particularly pursued and extreme enhancement on March 8 was persistently located adjacent to the epicenter and the magnetic conjugate point for a period long up to 16 h. Results from empirical and theoretical models verified that the solar effect is not enough to explain the observed TEC enhancement. Some other mechanisms may play a significant role in forming the significant TEC enhancement.

Anomalous magnetic variations after the 2011 Tohoku earthquake were observed by Hao *et al*.[80] from East Asia ground magnetometers. As some earlier works reported, the seismo-magnetic variations have obvious amplitude around the epicenter, it is interesting that notable variations were found at stations 2000–4000 km away from the epicenter, which is defined as Teleseismic Magnetic Disturbances (TMDs). TMDs appeared about 8 min later after the arrival of seismic Rayleigh waves and propagated at a horizontal velocity of 3.9 ± 0.1 km·s^{-1}. The wave-like TMDs lasted for no longer than 10 min and had a main period of 2.1–3.3 min. TMDs are not generated by direct effects of processes in focal area crust or tsunami waves; instead, their properties are consistent with the Rayleigh wave model of seismo-ionospheric disturbances. Therefore, the TMDs are the magnetic manifestation of Seismotraveling Ionospheric Disturbances (STIDs) generated by the acoustic waves launched by traveling Rayleigh waves through interaction between the ionosphere and atmosphere.

Hao *et al*.[81] provided evidence of quake-excited infrasonic waves during the Japan's Tohoku earthquake in terms of multi-instrument observations. The effects of surface oscillations were observed by local infrasonic detector, possibly due to surface oscillation-excited infrasonic waves, instead of direct influence of seismic vibration on the detector. Local excited infrasonic waves propagated upwards and the corresponding ionospheric disturbances were observed by Doppler shift measurements and GPS/TEC. All of these seismo-ionospheric effects observed by HF Doppler shift appeared after local arrivals of surface Rayleigh waves, with a time delay of 8–10 min, which is the time required for infrasonic wave to propagate upwards to the ionosphere.

Xu *et al*.[82] reported the disturbances in the ionosphere on 8 September 2010, 2 days before the Chongqing earthquake with a moderate $M_s = 4.7$ (29.4°N, 105.5°E, depth = 7.0 km, occurred at 21:21 LT). Observations of ground-based ionosondes and IGS receivers showed significant enhancements in f_0F_2 and TEC in the afternoon of 8 September 2010, with a limited area close to the epicenter. The observed enhancements were very likely associated with the forthcoming moderate earthquake, implying the possible coupling between ionospheric disturbances and earthquakes.

Liu *et al*.[83] studied the ionospheric perturbations before 82 M_s P 7.0 earthquakes during 2005–2010 by analyzing the DEMETER electron density (N_e) and temperature (T_e) observations. Disturbances in plasma parameters appeared before 49 earthquakes, with higher possibility for the shallow-focus earthquakes. Little difference was found between continental and oceanic earthquakes. Perturbations were seen spread on days before earthquakes and 1 day after earthquakes. The anomalies before earthquakes shifted equatorward from the epicenters.

9 Methodology Progress

Han and Wan[84] proposed an ionogram inversion method to retrieve the electron density profile, $N_e(h)$, of the Martian ionosphere. The ionograms were measured by the Mars Advanced Radar for Subsurface and Ionosphere Sounding (MARSIS) instrument on board the Mars Express. The inversion technique is modified from Titheridge's method by replacing the prior polynomials with EOFs, which are estimated from the archived RO $N_e(h)$ observations of the Mars Global Surveyor. Retrieval tests show the EOF-based technique of rapid converges and good stability. The new method provides an alternative tool to process the MARSIS ionograms.

Using the Sanya VHF radar observations carried out with coherent backscatter and specular meteor modes alternatively, Li *et al*.[85] compared the lower thermospheric winds obtained from Range Spread meteor Trail Echoes (RSTEs) and specular meteor trail echoes. The height profiles of neutral winds derived from both RSTEs and specular meteor trail echoes show similar patterns. Thus, lower thermospheric winds can be estimated from RSTEs with the Sanya coherent backscatter radar.

Liu *et al*.[86] carried out a Computed Tomography (CT) reconstruction of the topside ionosphere and plasmasphere (450 to 5000 km) based on GRACE-borne GPS TEC measurements. It is an efficient way to obtain

the 2-D profile of electron density from CT reconstruction based on the LEO-GPS data. Some reconstructed plasmasphere electron densities are generally unevenly distributed with latitude. Some interested phenomena have been detected in low and equatorial regions, including local enhanced density clusters in the plasmasphere, and column-like enhanced structures usually extending from the topside ionosphere up to the plasmasphere almost perpendicular to the magnetic field lines.

The ionospheric Computerized Tomography (CT) is an under-determined and ill-posed inverse problem. The constraint of limited-angle geometry and sparse receivers severely limits the precision and reliability of the CT imaging, especially in the vertical direction. Zhao *et al.*[87] put forward a method for combining vertical and oblique sounding data with the TEC retrieved from a tri-band beacon of a planned Chinese satellite for seismological studies. The initial bottomside profile takes the vertical/oblique observation, and the topside uses the Chapman layer. The attempts show that precision of the reconstructed electron density is significantly improved when the combined data are used, compared to that only from the three-frequency technique TEC.

Zhang *et al.*[88] studied the features of the temporal variation of Differential Code Biases (DCB). Besides the satellite DCB data from the Center for Orbit Determination in Europe (CODE) from 1999 to 2011, they also estimated DCB. They classified three types of variations in DCB at different time scales, day-to-day, annual and monotonously descending tendency from 1999 to 2010. The day-to-day and annual variations of the estimated GPS DCB are related to the ionospheric variability. The variation of DCBs on solar cycle time scale mixes the real hardware DCBs and pseudo-DCBs induced by ionospheric variation.

Detecting Doppler frequency shifts from ionospheric high frequency echoes is an efficient way to study ionospheric disturbances. Chen *et al.*[89] developed a new technique to detect ionospheric disturbances through combining the coded pulses and echo phase measurement analysis. They developed this on the Canadian Advanced Digital Ionosonde (CADI) platform. The mode can acquire accurate Doppler ionogram (Dopplionogram) and obtain the velocity of ionospheric disturbances in real time, which opens a new and effective way to enhance the ability of the available ionospheric instruments to monitor ionospheric information.

Ionograms are always contaminated by noises. Chen *et al.*[90] obtained high-quality ionograms with a curvelet transform denoising algorithm, which is based on image processing and can well preserve information about the layer traces. They proposed an adaptive threshold based on Bayes theory to improve the performance of the method. The curvelet transform method is combined with the traditional method to deal with a variety of noise for practical ionogram denoising. It can be used for ionogram automatic scaling.

Automatic scaling of ionograms is fundamental for obtaining ionospheric information. Chen *et al.*[91] proposed a new algorithm to scale F layer traces and recognize ordinary ray and extraordinary ray traces separately from ionograms in an automatic way. The method is developed from mathematical morphology, graph theory, and the echo characteristics of the ionosphere.

The vertical sounding has the advantage of easy providing many key ionospheric parameters, and the oblique ionosonde has the ability to detect wider regions. Chen *et al.*[92] conducted an experimental comparison between oblique and vertical detections in the EIA region of south China on 25 and 26 August 2010. The oblique detecting path was from Wuhan to Shenzhen and the VI ionosonde was set at the midpoint of the oblique path. The oblique ionogram reversion showed that both techniques provide comparable critical frequency, minimum virtual height and electron density profile.

To improve the spatial resolution of ionospheric tomography, Li *et al.*[93] combined simultaneous observations from space-based GPS onboard LEO satellites and from ground-based GPS to retrieve the image of Ionospheric Electron Density (IED). High precision dual-frequency GPS data were taken from the Crustal Movement Observation Network of China and several International GPS Service stations, LEO GPS data were from the COSMIC. Some retrieved IED profiles were compared with the COSMIC RO data, which were processed by COSMIC Data Analysis and Archival Center. Validations showed that N_mF_2 agrees with the ionosonde data. They also discussed the imaging effectiveness and potential benefits of including the COSMIC data into the IED inversion.

Cheng *et al.*[94] reported an EISCAT ionospheric heating experiment carried out on 13 September 2010 at Tromsø, Norway. Long-lasting enhanced ion- and plasma-lines were observed by the VHF incoherent scatter radar. The VHF data show that the enhanced ion-lines were descending in altitude with time during the heater-on period. The enhanced lines may be caused by Parametric Decay Instability. They gave a possible mechanism for the altitude evolution.

Zhang *et al.*[95] proposed a method for extracting

line-of-sight ionospheric observables (PIOs) from GPS data using precise point positioning. The PIOs have identical form with their counterparts obtained from leveling the geometry-free GPS carrier-phase to code (Leveling Ionospheric Observables, LIOs), and are affected by the satellite and receiver Inter-Frequency Biases (IFBs). They assessed the effects of extracting error arising from different sources on the PIOs and the LIOs, and verified the considerably reduced effects on the PIOs with respect to the LIOs.

The Super Dual Auroral Radar Network (SuperDARN) radars receive scatter both from ionospheric E- and F-region irregularities and from the Earth's surface. The current SuperDARN standard software determines the ionospheric scatter through assuming a straight-line propagation from the radar to the scattering zone with an altitude assigned by a standard height model. However, the knowledge of the group delay to a scatter volume is not sufficient for exact determination of the location of the irregularities. Liu *et al*.[96] evaluated the difference of the location of backscatter echoes between those determined by SuperDARN standard software and by ray tracing. Then they proposed an adjusted fitting location model using slant range and elevation angle to increase the reliability of location determining.

Liu *et al*.[97] analyzed the 241 days echoes of Zhongshan HF radar. The echoes have obvious diurnal variation and significantly influenced by geomagnetic activity. The echo occurrence peaks at dayside during geomagnetic quiet times. It shifts toward nightside. The average l-o-s velocity has obvious diurnal variation, with positive velocity at nightside and negative one at dayside. The average power and the l-o-s velocity are apparently higher under geomagnetic active conditions than during quiet times. The occurrence decreases obviously and spectral width becomes narrower with increasing geomagnetic level.

Shi *et al*.[98] presented a sounding rocket experiment conducted at Hainan. The sounding rocket was launched in the morning (06:15 LT) on 7 May 2011. A valley is observed in the ionospheric electron density profile between the E layer and F layer. Electron density outside the valley agrees with the simultaneous DPS-4 observation at the same location. They gave the value of the width, depth and altitude of the valley.

Acknowledgements

Libo Liu is gratified greatly for many colleagues providing their articles in preparing this report. This research was supported by National Natural Science Foundation of China (41231065), and the projects of Chinese Academy of Sciences (KZZD-EW-01-3), National Key Basic Research Program of China (2012CB825604).

REFERENCES

[1] Le H, Liu L, Chen Y, Wan W. Statistical analysis of ionospheric responses to solar flares in the solar cycle 23 [J]. *J. Geophys. Res. Space Phys.*, 2013, **118**: 576-582

[2] Xiong B, Wan W, Ning B, *et al.* A statistic study of ionospheric solar flare activity indicator [J]. *Space Weather*, 2014, 12, doi: 10.1002/2013SW001000

[3] Yue X, Schreiner W S, Kuo Y, *et al.* The effect of solar radio bursts on the GNSS radio occultation signals [J]. *J. Geophys. Res. Space Phys.*, 2013, **118**: 5906-5918

[4] Ma R, Xu J, Wang W, Lei J. The effect of ~27 day solar rotation on ionospheric F_2 region peak densities (N_mF_2) [J]. *J. Geophys. Res.*, 2012, **117**, A03303, doi: 10.1029/2011JA017190

[5] Chen Y, Liu L, Wan W. The discrepancy in solar EUV-proxy correlations on solar cycle and solar rotation timescales and its manifestation in the ionosphere [J]. *J. Geophys. Res.*, 2012, **117**, A01313, doi: 10.1029/2011JA017224

[6] Liu L, Yang J, Le H, *et al.* Comparative study of the equatorial ionosphere over Jicamarca during recent two solar minima [J]. *J. Geophys. Res.*, 2012, **117**, A01315, doi: 10.1029/2011JA017215

[7] Yang J, Liu L, Chen Y, Le H. Does the equatorial ionospheric peak electron density really record the lowest during the recent deep solar minimum [J]. *Chin. J. Geophys*., 2012, **55**: 2826-2834 (in Chinese)

[8] Wan W, Ren Z, F Ding, *et al.* A simulation study for the couplings between DE3 tide and longitudinal WN4 structure in the thermosphere and ionosphere [J]. *J. Atmos. Sol.Terr. Phys.*, 2012, **90/91**: 52-60

[9] Ren Z, Wan W, Liu L, Le H. TIME3D-IGGCAS: A new three-dimension mid- and low-latitude theoretical ionospheric model in realistic geomagnetic fields [J]. *J. Atmos. Sol. Terr. Phys.*, 2012, **80**: 258-266

[10] Xiong C, Lühr H. Nonmigrating tidal signatures in the magnitude and the inter-hemispheric asymmetry of the equatorial ionization anomaly [J]. *Ann. Geophys*., 2013, **31**: 1115-1130

[11] Xiong J, Wan W, Ding F, *et al.* Coupling between mesosphere and ionosphere over Beijing through semidiurnal tides during the 2009 sudden stratospheric warming [J]. *J. Geophys. Res. Space Phys.*, 2013, **118**: 2511-2521

[12] Mo X H, Zhang D H, Goncharenko L P, *et al.* Quasi-16-day periodic meridional movement of the equatorial ionization anomaly [J]. *Ann. Geophys*., 2014, **32**: 121-131

[13] Luan X, Dou X, Lei J, Jiang G. Terdiurnal migrating-tide signature in ionospheric total electron content [J]. *J. Geophys. Res*., 2012, **117**, A11302, doi: 10.1029/2012JA018199

[14] Gong Y, Zhou Q, Zhang S. Atmospheric tides in the low-latitude E and F regions and their responses to a sudden stratospheric warming event in January 2010 [J]. *J. Geophys. Res. Space Phys.,* 2013, **118**: 7913-7927

[15] Tang W, Xue X H, Lei J, Dou X K. Ionospheric quasi-biennial oscillation in global TEC observations [J]. *J. Atmos. Sol. Terr. Phys*., 2014, **107**: 36-41

[16] Hao Y Q, Zhang D H. Ionospheric absorption and planetary wave activity in East Asia sector [J]. *Sci. China: Tech. Sci.*, 2012, **55**: 1264-1272

[17] Chong X, Zhang M L, Zhang S R, *et al.* An investigation on plasmaspheric electron content derived from ISR and GPS observations at Millstone Hill [J]. *Chin. J. Geophys*., 2013, **56**(3): 738-745 (in Chinese)

[18] Wang H, Lühr H. Seasonal variation of the ion upflow in the topside ionosphere during SAPS (subauroral polarization stream) periods [J]. *Ann. Geophys*., 2013, **31**: 1521-1534

[19] Zhao M X, J Y Lu. Nonlinear dispersive scale Alfven waves in magnetosphere-ionosphere coupling: Physical processes and simulation results [J]. *Chin. Sci. Bull*, 2012, **57**: 1384-1392

[20] Zhao B, Wang M, Wang Y, *et al.* East-west differences in F-region electron density at midlatitude: Evidence from the Far East region [J]. *J. Geophys. Res*., *Space Phys.*, 2013, **118**: 542-553

[21] Xu J, Li X, Liu Y, Jing M. Effects of declination and thermospheric wind on TEC longitude variations in the mid-latitude ionosphere [J]. *Chin. J. Geophys.*, 2013, **56**: 1425-1434

[22] Xu J, Ma R, Wang W. Terannual variation in the F2 layer peak electron density (N_mF_2) at middle latitudes [J]. *J. Geophys. Res*., 2012, **117**, DOI: 10.1029/2011JA017191

[23] Chen Y, Liu L, Wan W, Ren Z. Equinoctial asymmetry in solar activity variations of NmF2 and TEC [J]. *Ann. Geophys.*, 2012, **30**: 613-622

[24] Xiong C, Lühr H, Ma S Y. The magnitude and inter-hemispheric asymmetry of equatorial ionization anomaly-based on CHAMP and GRACE observations [J]. *J. Atmos. Sol. Terr. Phys*., 2013, **105**: 160-169

[25] Huang L, Huang J, Wang J, *et al.* Analysis of the north-south asymmetry of the equatorial ionization anomaly around 110°E longitude [J]. *J. Atmos. Sol. Terr. Phys.*, 2013, **102**: 354-361

[26] Wu Y W, Liu R Y, Zhang B C, *et al.* Variations of the ionospheric TEC using simultaneous measurements from the China Crustal Movement Observation Network [J]. *Ann. Geophys*., 2012, **30:** 1423-1433

[27] Xiong C, Lühr H, Ma S Y. The subauroral electron density trough: Comparison between satellite observations and IRI-2007 model estimates [J]. *Adv. Space Res.*, 2013, **51**: 536-544

[28] Xiao Z, Yu S M, Shi H, *et al*. A brief of recent research progress on ionospheric disturbances [J]. *Sci. China Inf. Sci.*, 2013, **56**: 1-9

[29] Song Q, Ding F, Wan W, Ning B, Liu L. Global propagation features of large-scale traveling ionospheric disturbances during the magnetic storm of 7–10 November 2004 [J]. *Ann. Geophys.*, 2012, **30**: 683-694

[30] Song Q, Ding F, Wan W, *et al*. Monitoring traveling ionospheric disturbances using the GPS network around China during the geomagnetic storm on 28 May 2011 [J]. *Sci. China: Earth Sci.*, 2013, **56**: 718-726

[31] Ding F, Wan W, *et al*. Two-dimensional imaging of large-scale traveling ionospheric disturbances over China based on GPS data [J]. *J. Geophys. Res.*, 2012, **117**, A08318, doi: 10.1029/2012JA017546

[32] Ding F, Wan W, Ning B, *et al.* Observations of poleward-propagating large-scale traveling ionospheric disturbances in southern China [J]. *Ann. Geophys*., 2013, **31**: 377-385

[33] Ding F, Wan W, Li Q, *et al.* Comparative climatological study of large-scale traveling ionospheric disturbances over North America and China in 2011–2012 [J]. *J. Geophys. Res. Space Phys.,* 2014, **119**, doi*:* 10.1002/2013JA019523

[34] Song Q, Ding F, Wan W, *et al.* Statistical study of large-scale traveling ionospheric disturbances generated by the solar terminator over China [J]. *J. Geophys. Res. Space Phys.*, 2013, **118:** 4583-4593

[35] Cai H T, Yin F, Ma S Y, *et al*. Simultaneous observations of large-scale traveling ionospheric disturbances on the nightside and dayside middle latitude [J]. *Ann. Geophys.*, 2012, **30:** 1709-1717

[36] Sun S J, Ban P P, Chen C, *et al.* On the vertical drift of ionospheric F layer during disturbance time: Results from ionosondes [J]. *J. Geophys. Res. Space Phys.*, 2012, **117**, DOI: 10.1029/2011JA017106

[37] Zhao B, Wan W, Lei J *et al.* Positive ionospheric storm effects at Latin America longitude during the superstorm of 20–22 November 2003: revisit [J]. *Ann. Geophys.,* 2012, **30**: 831-840

[38] Wu Y W, Liu R Y, Zhang B C, *et al.* Multi-instrument observations of plasma features in the Arctic ionosphere during the main phase of a geomagnetic storm in December 2006 [J]. *J. Atmos. Sol. Terr. Phys*., 2013, **105**: 358-366

[39] Luan X, Wang W, Lei J, *et al*. Geomagnetic and auroral activity driven by corotating interaction regions during the declining phase of Solar Cycle 23 [J]. *J. Geophys. Res. Space Phys.*, 2013, **118**, doi: 10.1002/jgra.50195

[40] Liu J, Liu L, Zhao B, *et al*. Superposed epoch analyses of thermospheric response to CIRs: Solar cycle and seasonal dependencies [J]. *J. Geophys. Res.*, 2012, **117**, A00L10, doi: 10.1029/2011JA017315

[41] Liu J, Liu L, Zhao B, *et al.* High-speed stream impacts on the equatorial ionization anomaly region during the deep solar minimum year 2008 [J]. *J. Geophys. Res.*, 2012, **117**, A10304, doi: 10.1029/2012JA018015.

[42] Liu J, Liu L, Zhao B, Wan W. Influence of interplanetary solar wind sector polarity on the ionosphere [J]. *J. Geophys. Res.*, 2012, **117**, A08335, doi: 10.1029/2012JA017859

[43] Zhang D H, Mo X H, *et al*. Case study of ionospheric fluctuation over mid-latitude region during one large magnetic storm [J]. *Sci. China : Tech. Sci.*, 2012, **55**: 1198-1206

[44] Wang M, Lou W, Li P, *et al*. Monitoring the ionospheric storm effect with multiple instruments in North China: July 15-16, 2012 magnetic storm event [J]. *J. Atmos. Sol. Terr. Phys*., 2013, **102**: 261-268

[45] Xiao R, Xu J, Ma S, *et al.* Abnormal distribution of ionospheric electron density during November 2004 super-storm by 3D CT reconstructions from IGS and LEO/GPS observations [J]. *Sci. China: Tech. Sci.*, 2012, **55**: 1230-1239

[46] Xiong C, Lühr H, Ma S Y, *et al.* Features of highly structured equatorial plasma irregularities deduced from CHAMP observations [J]. *Ann. Geophys*., 2012, **30**: 1259-1269

[47] Ning B L, Hu G, Li L, *et al.* The first time observations of low-latitude ionospheric irregularities by VHF radar in Hainan [J]. *Sci. China: Tech.Sci.*, 2012, **55**: 1189-1197

[48] Ning B, Li G, Hu L, *et al.* Observations on the field-aligned irregularities using Sanya VHF radar: 1. Ionospheric E-region continuous echoes [J]. *Chin. J. Geophys.*, 2013, **56**: 719-730

[49] Li G, Ning B, Hu L, Li M. Observations on the field-aligned irregularities using Sanya VHF radar: 2. Low latitude Ionospheric E-region quasi-periodic echoes in the East Asian sector [J]. *Chin. J. Geophys.*, 2013, **56**: 2141-2151

[50] Hu L, Ning B, Li G, Li M. Observations on the field-aligned irregularities using Sanya VHF radar: 4. June solstitial F-region echoes in solar minimum [J]. *Chin. J. Geophys.*, 2014, **57**: 1-9

[51] Li G, Ning B, Hu L, *et al.* A comparison of lower thermospheric winds derived from range spread and specular meteor trail echoes [J]. *J. Geophys.Res*., 2012, **117**, A03310, doi: 10.1029/2011JA016847

[52] Li G, Ning B, Liu L, *et al.* Equinoctial and June solstitial irregularities over Sanya [J]. *Indian J.Radio Space Phys.*, 2012, **41**: 184-198

[53] Li G, Ning B, Abdu M A, *et al.* Precursor signatures and evolution of post-sunset equatorial spread-F observed over Sanya [J]. *J. Geophys. Res*., 2012, **117**, A08321, doi: 10.1029/2012JA017820

[54] Li G, Ning B, Abdu M A, *et al.* Longitudinal characteristics of spread F backscatter plumes observed with the EAR and Sanya VHF radar in Southeast Asia [J]. *J. Geophys. Res. Space Phys.*, 2013, 118, doi: 10.1002/jgra.50581

[55] Luo W, Xu J, Zhu Z. Theoretical modeling of the occurrence of equatorial and low-latitude ionospheric irregularity and scintillation [J]. *Chin. J. Geophys.*, 2013, **56**: 2892-2905

[56] Luo W, Xu J, Mao T. Investigation of hemispheric asymmetry and longitudinal variation of flux-tube integrated Rayleigh-Taylor instability [J]. *Chinese J. Geophys*., 2012, **55**: 1078-1087 (in Chinese)

[57] Xiong W, Xu J, Wang H, Xu L. Effect of temporal variation rate of cross polar cap potential on the equatorial ionospheric vertical drift: A statistical study [J]. *Sci.: China: Tech. Sci.*, 2012, **55**: 1217-1223

[58] Li G, Ning B, Patra A K, *et al.* On the linkage of daytime 150-km echoes and abnormal intermediate layer traces over Sanya [J]. *J. Geophys. Res. Space Physics*, 2013, **118**: 7262-7267

[59] Shi R. Study of the ionospheric Alfven resonant feed back instability [J]. *Chin. J. Geophys*. 2012, **55**: 744-750 (in Chinese)

[60] Ren Z, Wan W, Liu L, *et al.* Simulated mid-latitude summer nighttime anomaly in realistic geomagnetic fields [J]. *J. Geophys. Res.*, 2012, **117**, A03323, doi: 10.1029/2011JA017010.

[61] Ren Z, Wan W, Xiong J, Liu L. Simulated equinoctial asymmetry of the ionospheric vertical plasma drifts [J]. *J. Geophys. Res.*, 2012, **117**, A01301, doi: 10.1029/2010JA016952.

[62] Ren Z, Wan W, Liu L, Xiong J. Simulated longitudinal variations in the E-region plasma density induced by non-migrating tides [J]. *J. Atmos. Sol.Terr. Phys.*, 2012, **74**: 68-76

[63] Zhang M L, Liu L, Wan W, Ning B. An update global model of h_mF_2 from values estimated from ionosonde and COSMIC/FORMOSAT-3 radio occultation [J]. *Adv. Space Res.*, 2014, **53**: 395-402

[64] Yu Y, Wan W, Zhao B, *et al.* Modeling the global N_mF_2 from the GNSS derived TEC-GIMs [J]. *Space Weather*, 2013, **11**: 272-283.

[65] Wan W, Ding F, Ren Z, *et al.* Modeling the global ionospheric total electron content with empirical orthogonal function analysis [J]. *Sci. China: Tech. Sci.,* 2012, **55**: 1161-1168

[66] Ridley J, Xiao Z, Hao Y. A global model: Empirical orthogonal function analysis of total electron content 1999–2009 data [J]. *J. Geophys. Res*., 2012, **117**, A03328, doi: 10.1029/2011JA017238

[67] Liu J, Liu L, Zhao B, Wan W, Chen Y. Empirical modeling of ionospheric F_2 layer critical frequency over Wakkanai under geomagnetic quiet and disturbed conditions [J]. *Sci. China: Tech Sci.*, 2012, **55**: 1169-1177

[68] Sun S, Ban P, Chen C, Xu Z. An empirical correction model for low-latitude storm-time ionospheric foF2 considering the equatorial $E\times B$ drift [J]. *Adv. Space Res*., 2012, **49**: 1356-1362

[69] Zhao X, Ning B, Liu L, Song G. A prediction model of short-term ionospheric foF2 based on AdaBoost [J]. *Adv. Space Res.*, 2014, **53**: 387-394

[70] Wang S G, Shi J K, Wang X, *et al.* Correction of B2bot for NeQuick during low solar activity at Hainan station [J]. *Adv. Space Res.*, 2012, **49**: 1160-1166

[71] He F, Zhang B C, Huang D H. Averaged N_mF_2 of cusp-latitude ionosphere in northern hemisphere for solar minimum - Comparison between modeling and ESR during IPY [J]. *Sci China: Tech. Sci*, 2012, **55**: 1281-1286

[72] Shi R., Liu H, Yoshikawa A, Zhang B, Ni B. Coupling of electrons and inertial Alfven waves in the topside ionosphere [J]. *J. Geophys. Res. Space Phys.*, 2013, **118**, doi: 10.1002/jgra.50355

[73] Zhu Z, Chen K, Lan J, Sun F. F_3 layer feature under low and medium solar activity observed at a Chinese low latitude station Fuke [J]. *Adv. Space Res*., 2013, **52**: 383-390

[74] Zhu J, Zhao B, Wan W, Ning B. An investigation of the formation patterns of the ionospheric F3 layer in low and equatorial latitudes [J]. *J. Atmos. Sol. Terr. Phys.,* 2013, http: //dx.doi.org/10.1016/j.jastp.2013.04.015

[75] Liu L, Chen Y, Le H, *et al.* A case study of post-midnight enhancement in F-layer electron density over Sanya of China [J]. *J. Geophys. Res. Space Physics*, 2013, **118**: 4640-4648

[76] Chen G, *et al.*, Nighttime ionospheric enhancements induced by the occurrence of an evening solar eclipse [J]. *J. Geophys. Res. Space Phys*., 2013, **118**: 6588-6596

[77] Luan X, Dou X. Seasonal dependence of the longitudinal variations of nighttime ionospheric electron density and equivalent winds at southern midlatitudes [J]. *Ann. Geophys*., 2013, **31**: 1699-1708

[78] Ruan H, Lei J, Dou X, *et al.* Enhancements of nighttime neutral and ion temperatures in the F region over Millstone Hill [J]. *J. Geophys. Res. Space Phys.*, 2013, **118**, 1768-1776, doi: 10.1002/jgra.50202

[79] Le H, Liu L, Liu J Y, *et al.* The ionospheric anomalies prior to the M9.0 Tohoku-Oki earthquake [J]. *J. Asian Earth Sci.*, 2013, **62**: 476-484

[80] Hao Y Q, Xiao Z, Zhang D H. Teleseismic Magnetic Effects (TMDs) of 2011 Tohoku earthquake [J]. *J. Geophys. Res. Space Phys.*, 2013, **118**: 3914-3923

[81] Hao Y Q, Xiao Z, Zhang D H. Multi-instrument observation on co-seismic ionospheric effects after great Tohoku earthquake [J]. *J. Geophys. Res*., 2012, **117**, A02305, doi: 10.1029/2011JA017036

[82] Xu T, Hu Y, Zhang H, *et al.* Ionospheric disturbances on 8 September, 2010: Was it connected with the incoming moderate Chongqing earthquake [J]. *Adv. Space Res*., 2012, **50**: 205-210

[83] Liu J., J. Huang, and X. Zhang, Ionospheric perturbations in plasma parameters before global strong earthquakes [J]. *Adv. Space Res*., 2014, 53: 776-787

[84] Han X, Wan W. Ionogram inversion for MARSIS topside sounding [J]. *Earth Planets Space*, 2012, **64**: 753-757

[85] Li M, Li G, Ning B, Hu L. Observations on the field-aligned irregularities using Sanya VHF radar: 3. Range spread trail echoes [J]. *Chin. J. Geophys.*, 2013, **56**: 3969-3979

[86] Liu Y, Xu J, Xu L, Yin F, Ma S, Lühr H. Electron density distribution in the upper ionosphere and plasmasphere-CT imaging based on GRACE GPS data [J]. *Chin. J. Geophys.*, 2013, **56**: 2885-2891

[87] Zhao H, Xu Z, Wu Z, *et al.* A stable and fast method of ionospheric tomography by using diverse data sources [J]. *J. Atmos. Sol. Terr. Phys*., 2013, 97: 99-105

[88] Zhang D H, Shi H, Jin Y Q, *et al.* The variation of the estimated GPS instrumental bias and its possible connection with ionospheric variability [J]. *Sci. China: Tech. Sci.*, 2014, **57**: 67-79

[89] Chen K, Zhu Z, Ning B, *et al.* Developing a new mode for observation of ionospheric disturbances by digital ionosonde in ionospheric vertical sounding [J]. *Radio Sci*., 2012, **47**: RS3009, doi: 10.1029/2011RS004968.

[90] Chen Z, Wang S, Fang G, *et al*. Ionograms denoising via curvelet transform [J]. *Adv Space Res*., 2013, **52**: 1289-1296

[91] Chen Z, Wang S, Zhang S, *et al*. Automatic scaling of F layer from ionograms [J]. *Radio Sci*., 2013, **48**: 334-343

[92] Chen G, Zhao Z, Zhang Y, *et al.* Application of the oblique ionogram as vertical ionogram [J]. *Sci. China: Tech.Sci.*, 2012, **55**: 1240-1244

[93] Li H, Yuan Y, Li Z, *et al.* Ionospheric electron concentration imaging using combination of LEO satellite data with ground-based GPS observations over China [J]. *IEEE Trans. Geosci. Remote Sensing*, 2012, **50**: 1728-1734

[94] Cheng M, Xu B, Li H, *et al.* Observation of VHF incoherent scatter spectra disturbed by HF heating, Journal of Atmospheric and Solar-Terrestrial Physics [J]. 2013, **105-106**: 245-252

[95] Zhang B C, Ou J K, Yuan Y B, *et al.* Extraction of line-of-sight ionospheric observables from GPS data using precise point positioning [J]. *Sci. China: Earth Sci.*, 2012, **55**: 1919-1928

[96] Liu E X, Hu H Q, Liu R Y, *et al.* An adjusted location model for SuperDARN backscatter echoes [J]. *Ann. Geophys.*, 2012, **30**: 1769-1779

[97] Liu E, Hu H, Liu R, *et al*. Diurnal variation of the HF radar echoes at Zhongshan Station and the influence of geomagnetic activity [J]. *Chin. J. Geophys*. 2012: 3066-3076(in Chinese)

[98] Shi J K, Wang Z, Torkar K, *et al.* Ionospheric E–F valley observed by a sounding rocket at the low-latitude station Hainan [J]. *Ann. Geophys*., 2013, **31**: 1459-1462